1 # Structure of *Dunaliella* Photosystem II reveals conformational

2 # flexibility of stacked and unstacked supercomplexes

3

4 *Ido Caspy[1], Maria Fadeeva[1], Yuval Mazor[2,3]* and Nathan Nelson[1]***
5
6 *[1]Department of Biochemistry and Molecular Biology, The George S. Wise Faculty of Life*
7 *Sciences, Tel Aviv University, Tel Aviv, 69978, Israel*
8 *[2]School of Molecular Sciences, Arizona State University, Tempe, AZ, USA*
9 *[3]Biodesign Center for Applied Structural Discovery, Arizona State University, Tempe, AZ, USA*
10
11 ***Corresponding author**: ymazor@asu.edu*
12 *****Corresponding author**: nelson@tauex.tau.ac.il*

13 **Keywords**
14 photosynthesis, green algae, photosystem II, thylakoid, oxygen evolving complex, structure,
15 cryo-EM
16

17 ## Abstract

18 Photosystem II (PSII) generates an oxidant whose redox potential is high enough to enable water

19 oxidation[1,2], a substrate so abundant that it assures a practically unlimited electron source for life

20 on earth[3]. Our knowledge on the mechanism of water photooxidation was greatly advanced by

21 high-resolution structures of prokaryotic PSII[4–6]. Here we show high-resolution structures of

22 eukaryotic PSII from the green algae *Dunaliella salina* at two distinct conformations. The

23 conformers are also present in stacked PSII, exhibiting flexibility that is relevant to the grana

24 formation in chloroplasts of the green lineage. CP29, one of PSII associated light harvesting

25 antennae, plays a major role in distinguishing the two conformations of the supercomplex. We also

26 show that the stacked PSII dimer, a form suggested to support the organization of thylakoid

27 membranes[7,8], can appear in many different orientations providing a flexible stacking mechanism

28   for the arrangement of grana stacks in thylakoids. Our findings provide a structural basis for the

29   heterogenous nature of the eukaryotic PSII on multiple levels.

30   **Introduction**

31   In eukaryotes, the light reaction of oxygenic photosynthesis occurs in chloroplasts. Four protein

32   complexes essential for the light reactions reside in an elaborate membrane system of flattened

33   sacs called thylakoids[9]. From these four complexes the Photosystem II (PSII) complex catalyzes

34   light-driven water oxidation and provides the electrons used for carbon fixation[10,11].

35   Thylakoids form a physically continuous three-dimensional network, differentiated into two

36   distinct physical domains: cylindrical stacked structures (called grana) and connecting single

37   membrane regions (stroma lamellae). Photosystem I (PSI) is mainly located in the stroma lamellae

38   while PSII is found almost exclusively in the grana[12–14]. Grana stacking is a dynamic process

39   dependent on the internal osmotic pressure, the luminal ion composition, and environmental ques,

40   and is thought to be supported by interactions among PSII complexes[15–19].

41   PSII is a homodimer with a molecular mass of ~500 kDa, each monomer contains cofactors such

42   as chlorophylls (Chls), quinones, carotenoids, and lipids which are coordinated by at least 20

43   protein subunits[1,20]. In each PSII core, a cluster of four manganese (Mn) and one calcium (Ca)

44   carries out H_2O oxidation and O_2 release[21]. The eukaryotic reaction centre (RC) is a dimer

45   surrounded by tightly bound monomeric light harvesting complexes (LHCs) and trimeric LHCII

46   complexes[22–24]; Two monomeric LHCs, CP26 and CP29, are located between LHCII trimers and

47   PSII core subunits[25]; additional LHCII trimers can bind PSII depending on light intensity and

48   quality[26].

49   Although more than three billion years of evolution separate cyanobacteria, red algae, green algae

50   and plants, high resolution PSII structures show that each PSII monomer along with its dimeric

51 arrangement are highly conserved, especially in the membrane bound regions of the PSII[27–32].

52 Structural and spectroscopic investigations uncovered various aspects of PSII's water splitting

53 mechanism, but a complete model is still missing[4,5,33–35]. Most of the mechanistic and structural

54 studies of PSII were performed in thermophilic cyanobacteria, but structural studies of PSII from

55 the eukaryotic lineage are lagging[27,31,32,36].

56 In this work photosystem II was isolated from the halotolerant green alga *Dunaliella salina.* A

57 high-resolution (2.43 Å) structure of PSII shows unique structural properties of the *Dunaliella*

58 PSII supercomplex. The eukaryotic PSII appear to exist in two distinct core conformations that

59 differ substantially in their inner dimer separation and the location of CP29, an important

60 monomeric LHC. Structural analysis of stacked PSII dimers showed highly flexible interactions

61 which can play a role in the dynamic organisation of chloroplast membranes. These finding

62 introduce an additional, underlying, level of organisation which can impact its excitation energy

63 transfer properties and the overall organization of the thylakoid membranes.

64 **Results**

65 **Two distinct PSII conformation in green alga.**

66 Highly active PSII from *D. salina* cells was applied on glow-discharged holey carbon grids that

67 were vitrified for cryo-EM structural determination (see Methods). Initial classification of the

68 dataset showed that approximately 20% of the particle population were in a stacked PSII

69 configuration, containing two PSII dimers facing each other on their stromal side (**Extended Data**

70 **Fig. 1**). From the unstacked PSII dimers, approximately 20% were in the C2S configuration (two

71 Cores, one Stable LHCII), which was previously identified by low resolution cryo-EM[25]

72 (**Extended Data Fig. 1c**). The majority of the PSII particles contained 2 LHCII in the C2S2

73 configuration. The map of the C2S2 particles refined to a global resolution of 2.82 Å (**Extended**

74   **Data Fig. 2**). Close examination of this map revealed that CP29, one of the monomeric LHC

75   proteins, implicated as a junction for excitation energy transfer from LHCII trimers to PSII core,

76   appeared to be in lower resolution than the rest of the supercomplex (**Extended Data Fig. 2a**).

77   Indeed, when this particle set was further classified, two distinct PSII conformations of the PSII

78   supercomplex became apparent. In these two conformations the two PSII cores are shifted latterly

79   with respect to each other (**Fig. 1**). This lateral shift is accompanied by several other associated

80   movements, most noticeably, a large movement of the CP29 subunit (**Fig. 1**) in line with our initial

81   observation. The two conformers were denoted compact and stretched PSII ($C2S2_{COMP}$ and

82   $C2S2_{STR}$, respectively), and the high specific activity of 816 μmol O_2/mg Chl/h measured for the

83   preparation prior to vitrification suggest that both are highly active. The final reconstruction of the

84   compact orientation refined to an overall resolution of 2.43 Å, the highest of any eukaryotic PSII

85   structures (PDB ID 7PI0; **Fig. 1a** and **Extended Data Fig. 1-3**).
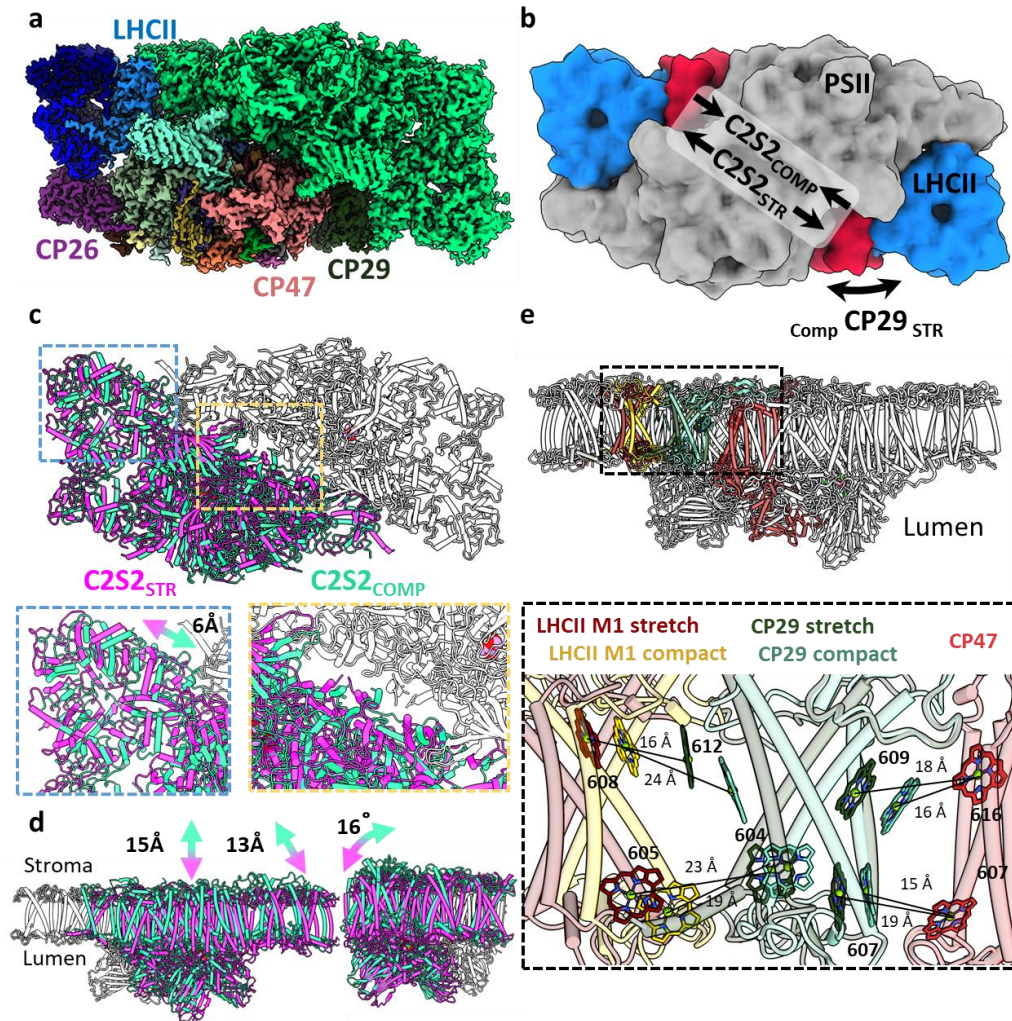
Fig. 1: Two conformation of the eukaryotic PSII. a. overall view of the PSII C2S2 map in the compact conformation. One asymmetric unit is colored in green, in the other each chain is colored individually. **b**. Low resolution model depicting the overall shifts in subunits between the two PSII conformations. CP29 in red, LHCII in blue and the two PSII cores in grey. **c**. The two PSII conformations were superposed on one asymmetric unit (colored in grey). The second asymmetric unit is colored in magenta for the stretched conformation (C2S2$_{STR}$) and green for the compact conformation (C2S2$_{COMP}$). A close up showing a 6 Å shift in the position of LHCII and the lateral displacement between the two cores. **d**. The stretched PSII conformation shows substantial drop in the membrane plane (13 to 15 Å, depending on the precise location), contributing to a larger inward curve (compared to the luminal space) of the entire supercomplex. Large deformations in the position of CP26 subunit which rotates by 16° between the two conformations. **e**. Considerable changes in the position of CP29 affect the transfer rates between LHCII and CP47. CP47 of both conformations (in red) is superposed and distances between key Chls of CP29$_{COMP}$ (light turquoise) and CP29$_{STR}$ (dark green) shows increased transfer distances in the stretched conformation. The distances between LHCII and CP29 follow an opposite trend, decreasing in the stretched conformation (LHCII$_{STR}$ in dark red) and increasing in the compact conformation (LHCII$_{COMP}$ in yellow).

The C2S2$_{COMP}$ structure is similar to the previously determined C2S2 supercomplex from

Chlamydomonas reinhardtii or higher plants[31,36] and the cyanobacterial core structures[4,6]. The

104 second, stretched conformer, was solved to 2.62 Å resolution, and accounted for about 37% of the

105 unstacked C2S2 PSII particles. **Fig. 1** and **Extended Data Movies 1-2** depict the superposition of

106 the polypeptide chains of the two conformers, showing major differences in the location and

107 orientation of PSII monomers. Superposition of the *Dunaliella* and *Chlamydomonas* C2S2 (PDB

108 6KAC) structures and maps suggests that the *Chlamydomonas* structure also contains these

109 different conformers. This may explain the decreased local map resolution presented in the

110 aforementioned subunits, compared to the rest of the cryo-EM map[31].

111 **Structures of *Dunaliella salina* unstacked PSII at high-resolution.**

112 Thus far, available PSII structures suggested a single, highly conserved organisation of the two

113 PSII cores[4,27–29,31,32]. The high-resolution structures of *Dunaliella* $C2S2_{COMP}$ and $C2S2_{STR}$ provide

114 a new perspective on the dynamic arrangement of eukaryotic PSII and the interaction of the core

115 complex with its LHCs. To compare the $C2S2_{COMP}$ and $C2S2_{STR}$, the core complexes were aligned

116 (**Fig. 1 and Extended Data Movies 1-2**). Initial inspection showed that one of the major

117 differences between the two conformations is the orientation of CP29 (**Fig. 1e**). In $C2S2_{STR}$ CP29

118 helices I and III move towards the LHCII trimer of the opposite monomer and away from CP47,

119 with helix II of CP29 serving as a rotation axis. Moreover, $CP29_{COMP}$ contained only 9 Chls,

120 compared to 11 in $CP29_{STR}$ and13 Chl in *Chlamydomonas* PSII CP29[31]. Chls 605 and 616 were

121 absent in both structures and $CP29_{COMP}$ was also missing Chls 611 and 613. This might be

122 attributed to the flexibility of CP29 C-terminus, or the internal rearrangement caused by its

123 movement.

124 In the $C2S2_{STR}$ conformation the PSII monomers slid in the membrane plane along the central

125 symmetry axis separating them (**Fig. 1b** and **Extended Data Movies 1-2**). The non-aligned core

126 shows the extent of the shift in the core peptides together with the minor LHCs and LHCII trimer

127   (**Fig.1c** and **d**). As a result, all the interactions at the cores interface are modified, leading to local

128   changes in chain orientations and the conformations of some loops. Core subunits at the centre of

129   the monomer displayed a greater shift (D1, D2, CP47 CP43 and PsbO were displaced by 6-10 Å;

130   **Fig. 1**), and the peripheral subunits showed the largest shift and tilt compared to C2S2$_{COMP}$ (PsbE,

131   PsbP and CP26 moved by 13 Å, PsbZ showed the largest relocation of nearly 15 Å. and CP26

132   showed a maximal tilt of 16º; **Fig. 1**). Multibody refinement[37] of both C2S2$_{COMP}$ and C2S2$_{STR}$

133   demonstrated that the two PSII monomers in each conformation contain additional structural

134   heterogeneity (**Extended Data Fig.4-5** and **Extended Data Movie 3-6**).

135   **Distinct CP29 conformations alter LHCII to PSII core connectivity**

136   The observed conformational change of CP29 alters excitation energy transfer (EET) pathways

137   from LHCII to the PSII core and may account for the differences between calculated and measured

138   EET[23,38–41]. To assess changes in transfer rates between the stretched and compact orientations, we

139   measured how the distances between the closest Chls of CP47 (PSII core), CP29 and LHCII change

140   between the two PSII conformations. The average distances between CP29 Chls 603, 607 and 609

141   to the CP47 Chls 607 and 616, changed from 17 Å to 20 Å between the compact to stretched

142   conformations, suggesting that faster transfer rates from CP29 to CP47 in the compact

143   conformation. In contrast to this, the distances between CP29 Chls 604 and 612 to LHCII Chls 604

144   and 608 increased from 20 Å in the compact conformation to 23 Å in the stretched conformation,

145   suggesting that transfer from LHCII to CP29 is slower in the compact orientation. The missing

146   CP29 Chls 611 and 613 form part of the interface to LHCII and are missing in the compact

147   conformation, which should also contribute to slower transfer rates from LHCII to CP29 in the

148   compact configuration (**Extended Data Fig. 6**). Altogether, transfer from LHCII to the PSII core

149   should be considerably slower in the compact orientation from both distance and Chl occupancy

150 considerations. Similar features of altered Chl conformations were identified in molecular

151 dynamics (MD) simulation of LHCII exploring its structural dynamics[42] compared to its crystal

152 structure. The analysis showed differences in the excitonic coupling of Chl clusters 606-607 and

153 611-612. MD suggested an increase in the interaction energies of 606-607 and a decrease in the

154 interaction energies of similar proportion in 611-612[42]. The 611-612 Chl pair was proposed as a

155 light-harvesting regulator of excitation energy transfer from CP29 to CP47 and as a quenching

156 site[38], as its change in fluorescence yield was attributed to a protein conformational change that

157 leads to a redistribution of the interpigment energetics[43].

158 The compact and stretched PSII conformation contain substantial levels of continuous

159 structural heterogeneity.

160 Using multibody refinement[37], with each PSII monomer defined as a separate rigid body,

161 significantly improved the resolution and map quality in both $C2S2_{COMP}$ and $C2S2_{STR}$, showing

162 that substantial structural heterogeneity exists in both datasets at the level of PSII monomers.

163 Analyzing the shape of the heterogeneity in $C2S2_{COMP}$ and $C2S2_{STR}$, using Principal Component

164 Analysis (PCA) showed that the first six Principal components (PCs) explains more than 85% of

165 the variance in the data and consists of continuous heterogeneity (**Extended Data Fig. 4-5;**

166 **Extended Data Movies 3-6**). Substantial displacements of approximately 13 Å are observed

167 between the two monomers in the compact conformation (**Extended Data Fig. 4**) and a larger

168 range of displacements (up to 20 Å) exists in the stretched conformation (**Extended Data Fig. 5**).

169 The direction of PCs describes translations perpendicular and parallel to the membrane plane. This

170 suggests that both conformations are flexible and can respond to different membrane curvature

171 (**Extended Data Movies 3-6**). To examine the possible effects on energy transfer we measured

172 the change in intermonomer Chl distances across the different components. As expected, the PCs

173 describing changes in the membrane plane significantly change some key distances between

174 LHCII, CP29 and D1 across monomers (**Fig. 2**). This means that within each PSII conformation,

175 substantial levels of heterogeneity in transfer rates should be considered. Changes in Chl positions

176 were observed in CP29 Chls linking CP29 to PSII core and those connecting CP29 with LHCII.

177 These Chls moved by an average distance of more than 5 Å, in both conformations (**Extended**

178 **Data Table 2**). This implies that the association between PSII monomers and between PSII cores

179 and LHCs contains a certain degree of freedom which can modulate excitation energy transfer, the

180 entire assembly may be affected by changes in thylakoid membrane properties such as fluidity,

181 composition, and curvature[44,45].

182
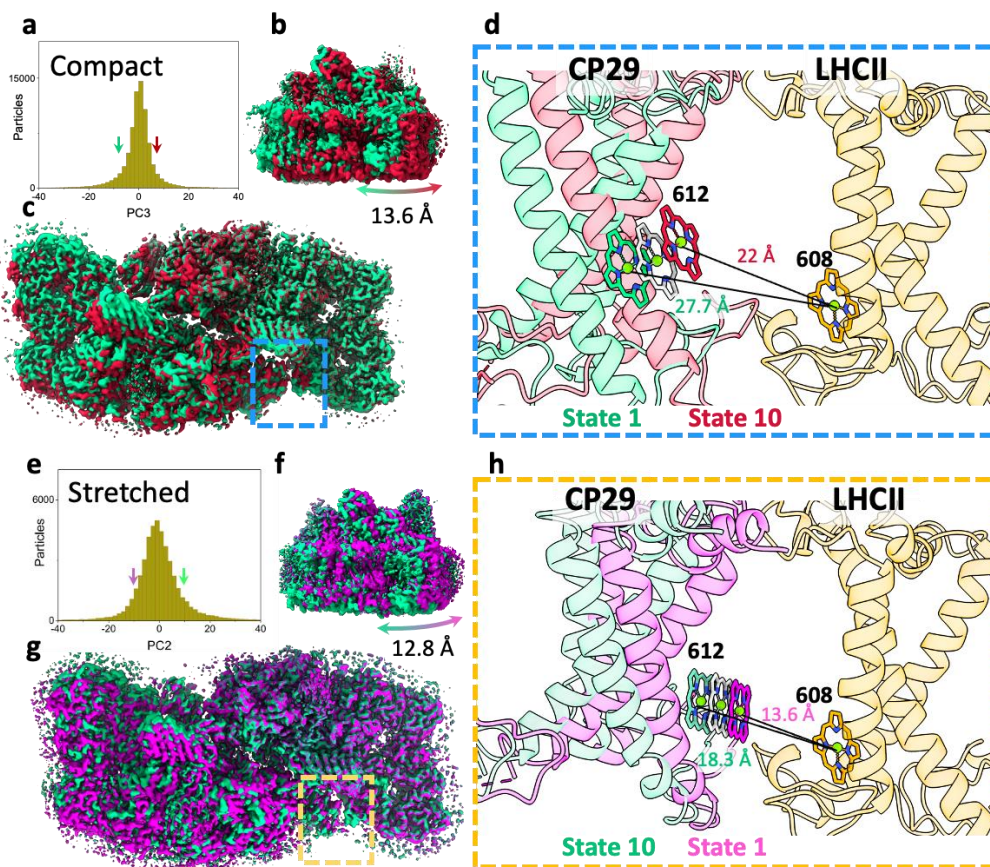
183
184 **Fig. 2: Heterogeneity within PSII states. a.** Continuous heterogeneity of C2S2$_{COMP}$ particles distribution
185 along the third principal component (PC) axis. Each PC was divided into ten states separated by nine percent
186 of the particle population along the PC axis. State 1 is marked with a green arrow and state 10 with a red

187   arrow. State 1 and 10 are coloured in green and red in panels a-d. **b.** To visualize the state differences, one
188   PSII monomer was superposed, and the other monomer was used to visualize the differences. Membrane
189   plane view of the shift in position of $C2S2_{COMP}$ in the third PC. **c.** Luminal view of the shift in position of
190    $C2S2_{COMP}$. CP29 and LHCII are marked with a blue rectangle **d.** Zoom-in on the change in CP29 position
191   between states 1 and 10. The change in distance between CP29 Chl 612 and LHCII M1 Chl 608 is shown.
192   LHCII M1 (from the superposed PSII monomer) is coloured light orange and the consensus position of Chl
193   612 is shown in grey. **e.** Continuous heterogeneity of $C2S2_{STR}$ particles distribution in the second PC. State
194   1 is marked with a magenta arrow and state 10 with a teal arrow. Colours are maintained in panels e-h. **f.**
195   Membrane plane view of the shift in position of $C2S2_{STR}$ in the second PC. **g.** Luminal view of the shift in
196   position of $C2S2_{STR}$. CP29 and LHCII are marked with an orange rectangle. **h.** Zoom-in on the change in
197   CP29 position between states 1 and 10. The change in distance between CP29 Chl 612 and LHCII M1 Chl
198   608 is shown. LHCII M1 is coloured orange and the consensus position of Chl 612 is shown in grey.
199
200   **Water channels and post-translational modifications in *Dunaliella* PSII**

201   More than 2100 water molecules were detected in the $C2S2_{COMP}$ model (**Fig. 3a-b**), the first

202   detailed water molecules structure for a eukaryotic PSII. Overall, water molecules are clearly

203   excluded from the membrane space in the PSII core, however the region occupied by LHC's show

204   a relatively high number of water molecules in the membrane region. This stems from the presence

205   of several conserved charged amino acids in these antennae and is probably important for the

206   inclusion of such hydrophilic residues within the membrane. We used CAVER[46] to analyze the

207   structure of internal cavities around the Oxygen Evolving Complex (OEC). As expected from the

208   highly conserved environment around the OEC, the water channels identified previously in the

209   high-resolution cyanobacterial core structure[5,47] are clearly visible in the eukaryotic PSII, and

210   overlap with the results of the internal cavity analysis, these are shown in **Fig. 3c** and named

211   "Large", "Narrow" and "Wide", following[47]. When analyzing the side chains lining the cavities

212   around the OEC, a small hydrophobic patch, highly conserved in prokaryotes and eukaryotes

213   (**Extend Data Fig. 7**), was identified at the beginning of the large channel (**Fig. 3d**). This

214   hydrophobic element may facilitate O_2 release as part of the catalytic cycle (**Fig. 3d**).

215
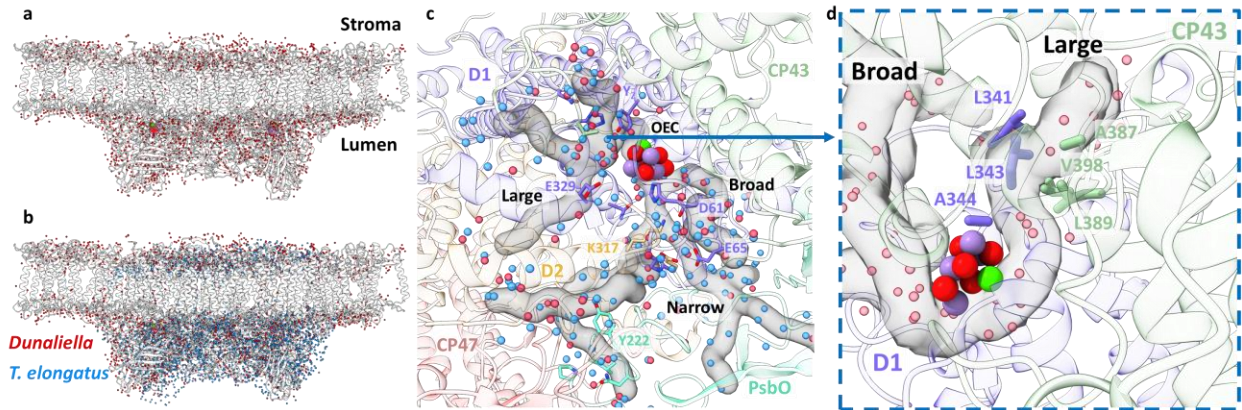
Fig. 3: Water distribution and channels in eukaryotic PSII. a. Water molecules distribution in *Dunaliella* C2S2$_{COMP}$ structure. The protein scaffold is coloured grey and water molecules are shown as red spheres. **b.** Water molecules distribution in *Dunaliella* C2S2$_{COMP}$ compared to *T. elongatus* PSII core (PDBID 3WU2). *T. elongatus* water molecules are shown as blue spheres. **c.** *Dunaliella* PSII water channels identified by CAVER analysis, shown as grey transparent maps. The Large, Narrow, and Broad channels are annotated along with selected amino acids coloured according to their respective subunits. Water molecules are presented as in panel b. **d.** A hydrophobic patch identified in the large channel near the OEC, which may serve as an O$_2$ release pathway. The region shown is indicated by the blue arrow, but the orientation is different to improve visualization.

225 Several unique map densities were identified during model building, close to the OEC of both

226 configurations a Na$^+$ ion was modeled. This Na$^+$ ion is coordinated by D1-His337, the backbone

227 carbonyls of D1-Glu333, D1-Arg334, D2-Asn350 and a water molecule, in agreement with the

228 recently identified[48] binding site (**Extended Data Fig. 8a-b**). This agrees with several studies

229 showing that Na$^+$ ions are required for optimal activity of PSII[48,49]. Two additional densities,

230 unique to C2S2$_{COMP,}$ were observed close to CP29-Ser84 and CP47-Cys218. These were modelled

231 as post-translational modifications (PTMs) – Ser84 appears to be phosphorylated and Cys218

232 seems to be sulfinylated (**Extended Data Fig. 8c-d**). Thus far, PTMs were structurally seen in

233 photosystems only as phosphorylated LHCII bound to PSI during state transition[50,51]. Although

234 they were not identified in-situ, several phosphorylation sites were shown to exist in CP29 large

235 stromal loop[52–55]. CP29 phosphorylation was suggested to be linked with various stress responses,

236 photosynthetic protein degradation and state transition. Cysteine sulfinylation was shown to be

237 linked to superoxide radical (O$_2^-$) accumulation, which is subsequently converted by superoxide

238   dismutase (SOD) to hydrogen peroxide (H_2O_2) molecules[56–58]. CP47-Cys218 is positioned on the

239   outer edge of PSII, close to the stromal end of the thylakoid membrane, and thus is susceptible to

240   oxidation by H_2O_2. The map density around Cys218 suggests two cysteine oxidation events which

241   result in the formation of sulfinic acid ($RS-O_2H$).

242   To summarize, the high-resolution structure of the eukaryotic PSII revealed two distinct states of

243   the PSII complex, adding a new dimension to the known, large compositional heterogeneity of this

244   important system[39,59,60]. The increased map resolution resulted in the identification of PTM's, and

245   several conserved hydrophobic residues near the OEC, which may serve as a pathway for the

246   release of O_2. In addition to the two distinct conformations, large levels of continuous structural

247   heterogeneity were discovered within each individual state. Multibody analysis[37] inherently treats

248   the data as a collection of rigid bodies. This is a good approximation of the heterogeneity in

249   photosynthetic systems but should be regarded as a conservative estimation to additional modes

250   of heterogeneity which exist in this system within each body[42].

251   **The structure of *Dunaliella salina* stacked PSII at high resolution.**

252   The thylakoid membrane is made of two spatially distinct regions, stroma lamellae and grana

253   stacks, each serving a different role in the photosynthetic process[61,62]. Grana stacks size and

254   numbers are affected by light intensity and ionic composition and can change rapidly[63]. Membrane

255   stacking depends on the presence of cations, mainly Mg^{2+}, which is abundant in the thylakoid

256   stroma[64], and between stacked PSII-LHCII[63]. In vitro, suspending chloroplast membranes in low-

257   salt medium causes grana unstacking, and addition of $MgCl_2$ reverts the membranes back to their

258   stacked organisation[65,66]. Several low-resolution cryo-EM models of stacked PSII were obtained

259   in recent years[67–69], but a high quality PSII structure that can shed light on the contribution of the

260   supercomplex to thylakoid membrane stacking is missing.

261 The stacked PSII dataset refined to a 3.68 Å map after applying multibody refinement, with each

262 dimer defined as a rigid body. Subsequently, the stacked particles were classified according to the

263 higher quality PSII dimer, and two distinct populations of stacked PSII dimers were obtained, as

264 observed for the unstacked PSII: one in the C2S2$_{COMP}$ conformation solved to 3.36 Å, and the

265 other in the C2S2$_{STR}$ conformation solved to 3.84 Å (**Fig. 4; Extended Data Fig. 9-10**). In both

266 classes the compact conformation exhibited the best fit for the second, lower resolution, PSII

267 dimer.
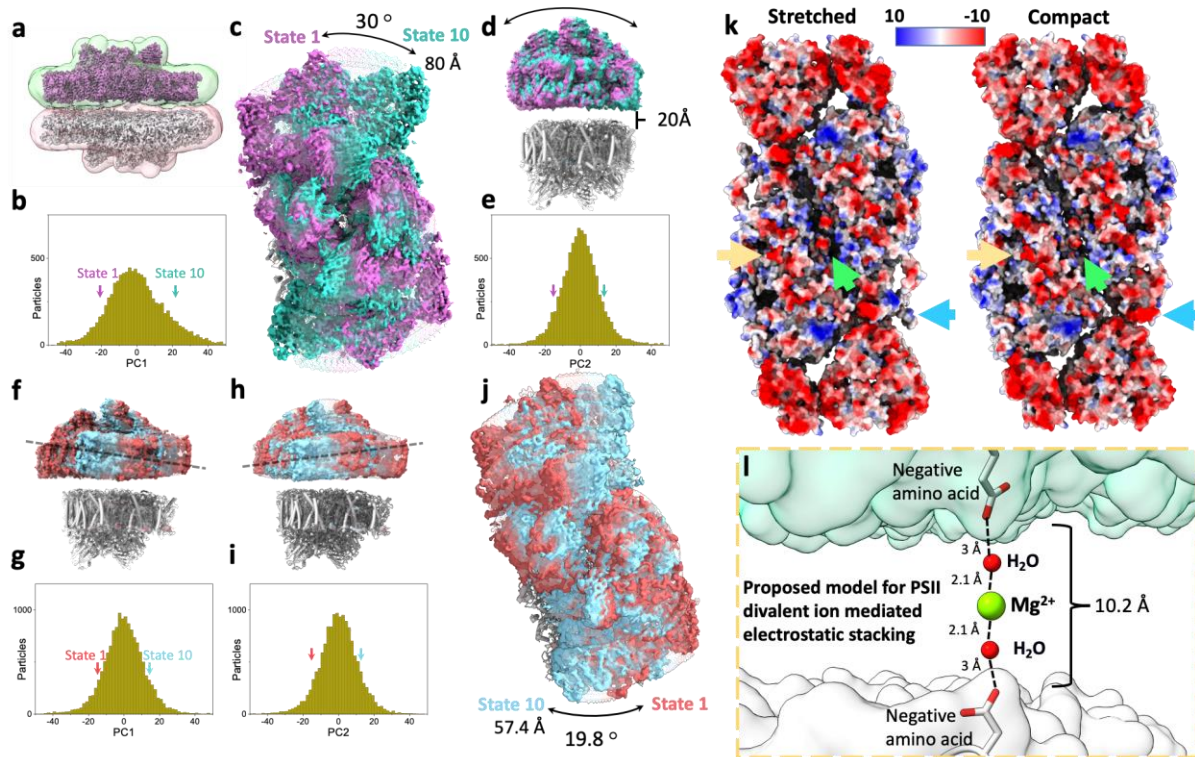
268

269 **Fig. 4: Heterogeneity, electrostatic interactions, and model for PSII stacking. a.** Stacked *Dunaliella*
270 PSII C2S2$_{COMP}$ maps, and the masks used for multibody refinement. Maps are coloured magenta and grey,
271 and masks in green and red. **b.** The particle distribution along the first PC shows continuous heterogeneity
272 in the stacked C2S2$_{COMP}$. State 1 is marked with a magenta arrow and state 10 with a teal arrow (colours
273 are preserved in panels b-e). **c.** Luminal view of the rotation of the upper PSII dimer between state 1 and
274 state 10 (the bottom dimer was kept in a fixed position). **d.** Membrane plane view of the shift in position of
275 the upper PSII dimer in C2S2$_{COMP}$ second PC. The distance between the upper and lower PSII is shown. **e.**
276 Particle distribution along the second PC of the stacked C2S2$_{COMP}$ shows continuous heterogeneity. **f.**
277 Membrane plane view of the tilt in the upper PSII dimer in C2S2$_{STR}$ particle set first PC. The direction of
278 the tilt is marked with a dashed line. State 1 is coloured red and state 10 in cyan (colours are preserved in

279 panels f-j). **g.** Continuous heterogeneity in the stacked C2S2$_{STR}$ particles distribution along the first PC. **h.**
280 Membrane plane view of the tilt in orientation of the upper PSII dimer in C2S2$_{STR}$ second PC (with the
281 bottom dimer kept fixed). The dashed line shows the tilt axis is opposite to that shown in panel f. **i.**
282 Continuous heterogeneity of stacked C2S2$_{STR}$ particles distribution in the second PC. **j.** Luminal view of
283 the rotation of the upper PSII dimer between state 1 and state 10. **k.** Coulombic electrostatic potential of
284 the stromal region of the stretched (left) and compact (right) conformations. Differences are marked for
285 CP47 C-terminus (orange arrow), the intermonomer space (green arrow) and CP29 (blue arrow). The
286 negative potentials (0 k_BT/e > Φ > -10 k_BT/e) are coloured red and positive potentials (0 k_BT/e < Φ < 10
287 k_BT/e) are coloured blue. **l.** Proposed model for PSII stacking mediated by negatively charged amino acids
288 and Mg^{2+} ions. Upper PSII shown as a green surface and the lower PSII as a white surface.

289 Roughly 20 Å separate the two stacked dimers in both classes, as previously shown[69]. In several

290 regions this value decreases to approximately 10 Å (**Fig. 4d** and **l**), owing to PSII stromal loops in

291 core subunits and LHCs protruding into the space between the two dimers. Both PSII dimers are

292 shifted by approximately 20 Å relative to each other rather than being perfectly aligned (**Fig. 4a**;

293 **Extended Data Fig. 11a**). PC analysis showed extensive displacements and rotations across the

294 population with stacked PSII dimers rotating relatively to their opposite dimer by as much as 30º,

295 and shifting by 80 Å in C2S2$_{COMP}$, while in C2S2$_{STR}$ the rotation is more restricted, showing a

296 maximum of 19.8º and a shift of 57 Å (**Fig. 4**). The rotation axis of C2S2$_{COMP}$ appears to be broad

297 region containing the N-termini stromal loops of D2 and CP29 on one dimer, and the stromal loop

298 connecting D2 helices IV and V, CP43 N-terminus, and the C-termini of CP43, CP47 and PsbI on

299 the opposite dimer (**Extended Data Fig. 11**). In the stacked C2S2$_{STR}$ these stacking interactions

300 also include a stromal loop from D1 which is pushed in the stromal gap by a change in the position

301 of the PsbT C-terminus (green arrow in **Fig. 4**), this shift pushes the D1 stromal loop (connecting

302 helices IV and V) into the stromal space and closer to the adjacent dimer (**Extended Data Fig.**

303 **11c**). On the axis of rotation which consists of PSII core subunits, additional interactions between

304 different LHCs seem to be essential to maintain stacking. All the rotation states include some

305 degree of LHCs interacting across the stromal gap between opposite PSII dimers and these seem

306 to limit the extent of possible rotational states. In the stacked C2S2$_{COMP}$ particle set the larger range

307   of rotations means that at the extreme states CP26 and LHCII M2 are not involved in stacking

308   interaction and can pair with additional complexes (**Extended Data Fig. 12a**), while in the stacked

309   C2S2$_{STR}$ particle set the smaller rotational range seem to be restricted by CP26 and LHCII M2

310   interactions (**Extended Data Fig. 12b**). These differences, when repeated over many stacked

311   complexes (with additional LHCII complexes) can translate into substantial changes in thylakoid

312   membrane stacking[70].

313   The closest contacts are found at the interface between core subunits from both PSII dimers and

314   CP29, supported by peripheral interactions between LHCII trimer and CP26. Most of the PSII

315   stromal surface is electronegative, and accordingly, most of the amino acids that seem to be

316   involved in stacking interactions are either negatively charged or uncharged (**Fig. 4k**). Interactions

317   spanning 10 Å are probably insufficient to maintain PSII in its stacked arrangement, however if

318   mediated by a Mg^{2+} ion and two-to-four H_2O molecules, stacking can be stabilized (**Fig. 4l**). These

319   interactions comply with the large degree of rotational freedom observed in the stacked dimers

320   and with the strong dependance of stacked dimers in the presence of Mg^{2+} ions and contribute to

321   thylakoid membrane stacking[66].

322   **Summary**

323   The structure of PSII from green algae revealed an unexpected level of conformational flexibility

324   in this highly conserved system. The two stable conformations appear to differ in their antennae

325   connectivity and should be considered in PSII modeling attempts. Within each state, the large

326   degree of structural heterogeneity also contributes to EET and may facilitate transitioning between

327   the different states. In the stacked PSII dimer we do not find any evidence for direct protein

328   interaction connecting the two stacked systems, instead, long range electrostatic interaction can

329   provide the sufficient flexibility needed for the dynamic behaviour of thylakoid membranes.

330   **Methods**

331   *Dunaliella* **PSII sample preparation:** After reaching an OD_{730} of 0.4, the culture was harvested

332   by centrifugation at 4,000 g for 10 min and resuspended in in a medium containing 50 mM

333   HEPES pH 7.5, 300 mM sucrose and 5 mM $MgCl_2$. The cells were washed ones in the same

334   buffer and suspended in a buffer containing 25 mM MES, pH 6.5, 10 mM CaCl2, 10 mM

335   MgCl2, 1 M betaine, 5 mM EDTA, 12.5% glycerol. Protease-inhibitors cocktail was added to

336   give final concentrations of 1mM PMSF, 1 µM pepstatin , 60 µM bestatin and 1mM

337   benzamidine. The cells were disrupted by an Avestin EmulsiFlex-C3 at 1,500 psi. Unbroken

338   cells and starch granules were removed by centrifugation at 5,000 g for 5min and the membranes

339   in the supernatant were precipitated by centrifugation in Ti70 rotor at 181,000 g for 1 h. The

340   pellet was suspended in a buffer containing 25 mM MES, pH 6.5, 10 mM $CaCl_2$, 10 mM $MgCl_2$,

341   1 M betaine, 5 mM EDTA, 12.5% glycerol giving a Chl concentration of 0.4 mg/ml. n-Decyl-**α**-

342   D-Maltopyranoside (α-DM) was added to a final concentration of 1% and following stirring for

343   30 min at 4^0C the insoluble material was removed by centrifugation of 10,000 g for 5 min.

344   Supernatant was concentrated by centrifugation in TI-75 rotor at 377,000 g for 80 minutes. The

345   pellet was suspended in the above buffer containing 0.3% α-DM at Chl concentration of about 1

346   mg/ml, loaded on sucrose gradients of 10 to 50% in SW-60 rotor and run at 336,000 g for 15 h.

347   **Extended Data Fig. 13a** shows the distribution of green bands in the tubes. The band containing

348   PSII was concentrated by centrifugation at 550,000 g for 2h and the pellet was suspended in a

349   buffer containing 25 mM MES (pH 6.5), 1 mM CaCl2, 5 mM MgCl2 and 0.1% α-DM to give a

350   Chl concentration of 2 mg Chl/ml. SDS-PAGE of the three bands is presented in **Extended Data**

351   **Fig. 13b.** The final preparation exhibited oxygen evolution activity of 816 µmole O_2/mg Chl/h

352   under 560 µmole photons $m^{-2}\,s^{-1}$ illumination **Extended Data Fig. 13c**.

353

354   **Cryo-EM data collection and processing:** Concentrated PSII solution (3 µl) was applied on

355   glow-discharged holey carbon grids (Cu Quantifoil R1.2/1.3) that were vitrified for cryo-EM

356   structural determination using a Vitrobot FEI (3 s blot at 4°C and 100% humidity). The images

357   were collected using a 300 kV FEI Titan Krios electron microscope, with a slit width of 20 eV

358   on a GIF-Quantum energy filter, at the EMBL cryo facility, Heidelberg, Germany. A Gatan

359   Quantum K3-Summit detector was used in counting mode at a magnification of 130,000

360   (yielding a pixel size of 0.64 Å), with a total dose of 51.81 e $Å^{-2}$. EPU was used to collect a total

361   of 13,586 images, which were dose-fractionated into 40 video frames, with defocus values of

362   0.8–1.9 µm at increments of 0.1 µm. The collected micrographs were motion-corrected and dose-

363   weighted using MotionCor2[71]. The contrast transfer function parameters were estimated using

364   CtfFind v.4.1[72]. A total of 401,467 particles were picked using LoG reference-free picking in

365   RELION3.1[73]. The picked particles were processed for reference-free two-dimensional (2D)

366   averaging. After several rounds of 2D classification, which resulted in 253,804 particles, two

367   initial model was generated using RELION3.1[73], for the unstacked and stacked PSII.

368   3D classification of the unstacked PSII revealed two organisations of the light-harvesting

369   complexes surrounding the core complex – C2S and C2S2. C2S contained 21,066 particles were

370   resampled at a pixel size of 0.896 Å, pooled together and processed for 3D homogeneous

371   refinement and multibody refinement[37] using RELION3.1[73], giving a final resolution of 3.61 Å.

372   The C2S2 configuration was comprised of 75,904 particles with a C2 symmetry, and these were

373   resampled at a pixel size of 0.896 Å, pooled together and processed for 3D homogeneous

374   refinement and postprocessing using RELION3.1[73], giving a final resolution of 2.82Å. In an

375   attempt to improve the map density of C2S2, mainly in the vicinity of CP29 and LHCII trimer,

376   3D classification without refinement was performed, and revealed two distinct C2S2

377   conformations – compact (C2S2$_{COMP}$) and stretched (C2S2$_{STR}$). C2S2$_{COMP}$ was composed of

378   39,357 particles that undergone symmetry expansion, 3D homogeneous refinement and

379   multibody refinement[37] in C1 symmetry to give a final resolution of 2.43 Å, and C2S2$_{STR}$ was

380   composed of 23,014 particles that undergone symmetry expansion, 3D homogeneous refinement

381   and multibody refinement[37] in C1 symmetry to give a final resolution of 2.62 Å.

382   23,874 particles that were assigned to the stacked PSII arrangement were resampled at a pixel

383   size of 0.96 Å, pooled together and processed for 3D homogeneous refinement and multibody

384   refinement[37][73] in C1 symmetry using RELION3.1[73] and yielded a final resolution of 3.68 Å.

385   Focused refinement on each individual PSII complex yielded similar resolutions before

386   multibody refinement (3.53 Å and 3.58 Å on each complex), showing both positions are

387   occupied roughly by the same number of complexes. Focused classification was carried out on

388   the upper dimer of the stacked PSII particles to determine if the compact and stretched

389   conformations were also present in the stacked PSII arrangement. This analysis showed that the

390   stacked PSII also contained a mixed population of the compact and stretched conformations. The

391   compact set was comprised of 9,567 particles, and these were pooled together and processed for

392   3D homogeneous refinement followed by multibody refinement[37] to give a final resolution of

393   3.36 Å. The stretched set comprised of 14,307 particles, these were pooled together and

394   processed for 3D homogeneous refinement followed by multibody refinement[37] to give a final

395   resolution of 3.84 Å. Performing focused refinement on the lower PSII dimer of both

396   conformations suggested a conformation mixture as well, but was less conclusive, due to the

397   lower map quality of the lower PSII dimer and both were fitted with the PSII$_{COMP}$ model (using

398   rigid body refinement) which gave the best overall fit to the map. All the reported resolutions

399   were based on a gold-standard refinement, applying the 0.143 criterion on the FSC between the

400   reconstructed half-maps. (**Extended Data Fig. 2**).

401

402   **Model building:** To generate the C2S2 PSII, the cryo-EM structure of the C2S2

403   *Chlamydomonas reinhardtii* PSII model PDB 6KAC[31] was selected. This model was fitted onto

404   the cryo-EM density map using phenix.dock_in_map in the PHENIX suite[74], and manually

405   rebuilt using Coot[75]. Stereochemical refinement was performed using phenix.real_space_refine

406   in the PHENIX suite[74]. The final model was validated using MolProbity[76]. The refinement

407   statistics are provided in **Extended Data Table 1**. Local resolution was determined using

408   ResMap[77], and the figures were generated using UCSF Chimera[78] and UCSF ChimeraX[79].

409   Representative cryo-EM densities are shown in **Extended Data Fig. 3**.

410

411   **Data availability:** The atomic coordinates have been deposited in the Protein Data Bank, with

412   accession code 7PI0 (C2S2$_{COMP}$), 7PI5 (C2S2$_{STR}$), 7PNK (C2S), 7PIN (stacked C2S2$_{COMP}$) and

413   7PIW (stacked C2S2$_{STR}$). The cryo-EM maps have been deposited in the Electron Microscopy

414   Data Bank, with accession codes EMD-13429 (C2S2$_{COMP}$), EMD-13430 (C2S2$_{STR}$), EMD-13548

415   (C2S), EMD-13444 (stacked C2S2$_{COMP}$) and EMD-13455 (stacked C2S2$_{STR}$).

416

417   **Acknowledgements**

430

Author Contributions

432 I.C., M.F., Y.M., and N.N. performed the research. I.C., Y.M, and N.N. analyzed the data. I.C.,

433 Y.M., and N.N. wrote the manuscript. All the authors discussed, commented on, and approved

434 the final manuscript.

435

Author Information

437 Correspondence and requests for materials should be addressed to N.N (nelson@tauex.tau.ac.il)

438 or Y.M (ymazor@asu.edu).

439

Competing interests

441 The authors declare that there are no competing interests.

442

References

444 1.   Shen, J. R. The structure of photosystem II and the mechanism of water oxidation in

445   photosynthesis. *Annu. Rev. Plant Biol.* **66**, 23–48 (2015).

446   2.   McEvoy, J. P. & Brudvig, G. W. Water-splitting chemistry of photosystem II. *Chemical*

447   *Reviews* vol. 106 4455–4483 (2006).

448   3.   Barber, J. Water, water everywhere, and its remarkable chemistry. *Biochim. Biophys. Acta*

449   *- Bioenerg.* **1655**, 123–132 (2004).

450   4.   Umena, Y., Kawakami, K., Shen, J. R. & Kamiya, N. Crystal structure of oxygen-

451   evolving photosystem II at a resolution of 1.9Å. *Nature* **473**, 55–60 (2011).

452   5.   Suga, M. *et al.* An oxyl/oxo mechanism for oxygen-oxygen coupling in PSII revealed by

453   an x-ray free-electron laser. *Science (80-.).* **366**, 334–338 (2019).

454   6.   Kato, K. *et al.* High-resolution cryo-EM structure of photosystem II reveals damage from

455   high-dose electron beams. *Commun. Biol. 2021 41* **4**, 1–11 (2021).

456   7.   Garab, G. & Mustárdy, L. Role of LHCII-containing macrodomains in the structure,

457   function and dynamics of grana. *Funct. Plant Biol.* **27**, 723–723 (2000).

458   8.   Kirchhoff, H. *et al.* Structural and functional self-organization of Photosystem II in grana

459   thylakoids. *Biochim. Biophys. Acta - Bioenerg.* **1767**, 1180–1188 (2007).

460   9.   Nelson, N. & Ben-Shem, A. The complex architecture of oxygenic photosynthesis. *Nature*

461   *Reviews Molecular Cell Biology* vol. 5 971–982 (2004).

462   10. Vinyard, D. J., Ananyev, G. M. & Charles Dismukes, G. Photosystem II: The reaction

463   center of oxygenic photosynthesis. *Annual Review of Biochemistry* vol. 82 577–606

464   (2013).

465   11. Nelson, N. & Junge, W. Structure and energy transfer in photosystems of oxygenic

466   photosynthesis. *Annual Review of Biochemistry* vol. 84 659–683 (2015).

467   12. Hankamer, B., Barber, J. & Boekema, E. J. Structure and membrane organization of

468   photosystem ii in green plants. *Annu. Rev. Plant Biol.* **48**, 641–671 (1997).

469   13.   Anderson, J. M. Changing concepts about the distribution of Photosystems I and II

470   between grana-appressed and stroma-exposed thylakoid membranes. *Photosynthesis*

471   *Research* vol. 73 157–164 (2002).

472   14.   Kim, E. H., Wah, S. C., Horton, P. & Anderson, J. M. Entropy-assisted stacking of

473   thylakoid membranes. *Biochim. Biophys. Acta - Bioenerg.* **1708**, 187–195 (2005).

474   15.   Rubin, B. T., Chow, W. S. & Barber, J. Experimental and theoretical considerations of

475   mechanisms controlling cation effects on thylakoid membrane stacking and chlorophyll

476   fluorescence. *BBA - Bioenerg.* **634**, 174–190 (1981).

477   16.   Barber, J., Chow, W. S., Scoufflaire, C. & Lannoye, R. The relationship between

478   thylakoid stacking and salt induced chlorophyll fluorescence changes. *BBA - Bioenerg.*

479   **591**, 92–103 (1980).

480   17.   Kirchhoff, H. Structural changes of the thylakoid membrane network induced by high

481   light stress in plant chloroplasts. *Philosophical Transactions of the Royal Society B:*

482   *Biological Sciences* vol. 369 (2014).

483   18.   Liu, X., Zhou, Y., Xiao, J. & Bao, F. Effects of chilling on the structure, function and

484   development of chloroplasts. *Frontiers in Plant Science* vol. 871 (2018).

485   19.   Dalal, V. K. & Tripathy, B. C. Water-stress induced downsizing of light-harvesting

486   antenna complex protects developing rice seedlings from photo-oxidative damage. *Sci.*

487   *Rep.* **8**, (2018).

488   20.   Cox, N., Pantazis, D. A. & Lubitz, W. Current Understanding of the Mechanism of Water

489   Oxidation in Photosystem II and Its Relation to XFEL Data. *Annu. Rev. Biochem.* **89**,

490   795–820 (2020).

491   21.   Nelson, N. & Yocum, C. F. Structure and function of photosystems I and II. *Annual*

492   *Review of Plant Biology* vol. 57 521–565 (2006).

493   22.   Daskalakis, V. Protein-protein interactions within photosystem II under photoprotection:

494   The synergy between CP29 minor antenna, subunit S (PsbS) and zeaxanthin at all-atom

495   resolution. *Phys. Chem. Chem. Phys.* **20**, 11843–11855 (2018).

496   23.   Mascoli, V., Novoderezhkin, V., Liguori, N., Xu, P. & Croce, R. Design principles of

497   solar light harvesting in plants: Functional architecture of the monomeric antenna CP29.

498   *Biochim. Biophys. Acta - Bioenerg.* **1861**, (2020).

499   24.   Barber, J., Nield, J. & Tommos, C. Organization of transmembrane helices in photosystem

500   II: Comparison of plants and cyanobacteria. in *Philosophical Transactions of the Royal*

501   *Society B: Biological Sciences* vol. 357 1329–1335 (Royal Society, 2002).

502   25.   Drop, B. *et al.* Light-harvesting complex II (LHCII) and its supramolecular organization

503   in Chlamydomonas reinhardtii. *Biochim. Biophys. Acta - Bioenerg.* **1837**, 63–72 (2014).

504   26.   Goldschmidt-Clermont, M. & Bassi, R. Sharing light between two photosystems:

505   Mechanism of state transitions. *Current Opinion in Plant Biology* vol. 25 71–78 (2015).

506   27.   Wei, X. *et al.* Structure of spinach photosystem II-LHCII supercomplex at 3.2 Å

507   resolution. *Nature* **534**, 69–74 (2016).

508   28.   Su, X. *et al.* Structure and assembly mechanism of plant C2S2M2-type PSII-LHCII

509   supercomplex. *Science (80-.).* **357**, 815–820 (2017).

510   29.   Pi, X. *et al.* The pigment-protein network of a diatom photosystem II–light-harvesting

511   antenna supercomplex. *Science (80-.).* **365**, (2019).

512   30.   Van Bezouwen, L. S. *et al.* Subunit and chlorophyll organization of the plant photosystem

513   II supercomplex. *Nat. Plants* **3**, 1–11 (2017).

514 31. Sheng, X. *et al.* Structural insight into light harvesting for photosystem II in green algae.

515   *Nat. Plants* **5**, 1320–1330 (2019).

516 32. Ago, H. *et al.* Novel features of eukaryotic photosystem II revealed by its crystal structure

517   analysis from a red alga. *J. Biol. Chem.* **291**, 5676–5687 (2016).

518 33. Cox, N. *et al.* Electronic structure of the oxygen-evolving complex in photosystem II prior

519   to O-O bond formation. *Science (80-.).* **345**, 804–808 (2014).

520 34. Kupitz, C. *et al.* Serial time-resolved crystallography of photosystem II using a

521   femtosecond X-ray laser. *Nat. 2014 5137517* **513**, 261–265 (2014).

522 35. Kern, J. *et al.* Structures of the intermediates of Kok's photosynthetic water oxidation

523   clock. *Nat. 2018 5637731* **563**, 421–425 (2018).

524 36. Shen, L. *et al.* Structure of a C2S2M2N2-type PSII–LHCII supercomplex from the green

525   alga Chlamydomonas reinhardtii. *Proc. Natl. Acad. Sci. U. S. A.* **116**, 21246–21255

526   (2019).

527 37. Nakane, T., Kimanius, D., Lindahl, E. & Scheres, S. H. W. Characterisation of molecular

528   motions in cryo-EM single-particle data by multi-body refinement in RELION. *Elife* **7**,

529   (2018).

530 38. Caffarri, S., Broess, K., Croce, R. & Van Amerongen, H. Excitation energy transfer and

531   trapping in higher plant Photosystem II complexes with different antenna sizes. *Biophys.*

532   *J.* **100**, 2094–2103 (2011).

533 39. Croce, R. & Van Amerongen, H. Light-harvesting and structural organization of

534   Photosystem II: From individual complexes to thylakoid membrane. *Journal of*

535   *Photochemistry and Photobiology B: Biology* vol. 104 142–153 (2011).

536 40. Croce, R. & van Amerongen, H. Light harvesting in oxygenic photosynthesis: Structural

537   biology meets spectroscopy. *Science* vol. 369 (2020).

538 41. Van Der Weij-De Wit, C. D., Dekker, J. P., Van Grondelle, R. & Van Stokkum, I. H. M.

539   Charge separation is virtually irreversible in photosystem II core complexes with oxidized

540   primary quinone acceptor. *J. Phys. Chem. A* **115**, 3947–3956 (2011).

541 42. Liguori, N., Periole, X., Marrink, S. J. & Croce, R. From light-harvesting to

542   photoprotection: structural basis of the dynamic switch of the major antenna complex of

543   plants (LHCII). *Sci. Rep.* **5**, (2015).

544 43. Valkunas, L., Chmeliov, J., Krüger, T. P. J., Ilioaia, C. & Grondelle, R. van. How

545   Photosynthetic Proteins Switch. *J. Phys. Chem. Lett.* **3**, 2779–2784 (2012).

546 44. Tardy, F. & Havaux, M. Thylakoid membrane fluidity and thermostability during the

547   operation of the xanthophyll cycle in higher-plant chloroplasts. *Biochim. Biophys. Acta -*

548   *Biomembr.* **1330**, 179–193 (1997).

549 45. Johnson, M. P. & Wientjes, E. The relevance of dynamic thylakoid organisation to

550   photosynthetic regulation. *Biochim. Biophys. Acta - Bioenerg.* **1861**, 148039 (2020).

551 46. Chovancova, E. *et al.* CAVER 3.0: A Tool for the Analysis of Transport Pathways in

552   Dynamic Protein Structures. *PLOS Comput. Biol.* **8**, e1002708 (2012).

553 47. Kaur, D. *et al.* Tracing the Pathways of Waters and Protons in Photosystem II and

554   Cytochrome c Oxidase. *Inorganics 2019, Vol. 7, Page 14* **7**, 14 (2019).

555 48. Wang, J. *et al.* Identification of a Na+-Binding Site near the Oxygen-Evolving Complex

556   of Spinach Photosystem II. *Biochemistry* **59**, 2823–2831 (2020).

557 49. Pogoryelov, D. *et al.* Sodium Dependency of the Photosynthetic Electron Transport in the

558   Alkaliphilic Cyanobacterium Arthrospira platensis. *J. Bioenerg. Biomembr.* **35**, 427–437

559   (2003).

560   50.   Pan, X. *et al.* Structure of the maize photosystem I supercomplex with light-harvesting

561   complexes I and II. *Science (80-.).* **360**, 1109–1113 (2018).

562   51.   Huang, Z. *et al.* Structure of photosystem I-LHCI-LHCII from the green alga

563   Chlamydomonas reinhardtii in State 2. *Nat. Commun.* **12**, 1100 (2021).

564   52.   Poudyal, R. S. *et al.* Combinatory actions of CP29 phosphorylation by STN7 and stability

565   regulate leaf age-dependent disassembly of photosynthetic complexes. *Sci. Rep.* **10**, 1–10

566   (2020).

567   53.   Chen, Y. E., Zhao, Z. Y., Zhang, H. Y., Zeng, X. Y. & Yuan, S. Significance of CP29

568   reversible phosphorylation in thylakoids of higher plants under environmental stresses.

569   *Journal of Experimental Botany* vol. 64 1167–1178 (2013).

570   54.   Jansson, H. *et al.* The crystal structure of the spinach plastocyanin double mutant

571   G8D/L12E gives insight into its low reactivity towards photosystem 1 and cytochrome f.

572   *Biochim. Biophys. Acta - Bioenerg.* **1607**, 203–210 (2003).

573   55.   Liu, W. J. *et al.* Dephosphorylation of photosystem II proteins and phosphorylation of

574   CP29 in barley photosynthetic membranes as a response to water stress. *Biochim. Biophys.*

575   *Acta - Bioenerg.* **1787**, 1238–1245 (2009).

576   56.   Sevilla, F. *et al.* The thioredoxin/peroxiredoxin/sulfiredoxin system: Current overview on

577   its redox function in plants and regulation by reactive oxygen and nitrogen species.

578   *Journal of Experimental Botany* vol. 66 2945–2955 (2015).

579   57.   Rey, P. *et al.* The Arabidopsis thaliana sulfiredoxin is a plastidic cysteine-sulfinic acid

580   reductase involved in the photooxidative stress response. *Plant J.* **49**, 505–514 (2007).

581   58.   Matamoros, M. A. & Becana, M. Molecular responses of legumes to abiotic stress: post-

582   translational modifications of proteins and redox signaling. *J. Exp. Bot.* (2021)

583   doi:10.1093/jxb/erab008.

584   59.   Caffarri, S., Kouřil, R., Kereïche, S., Boekema, E. J. & Croce, R. Functional architecture

585   of higher plant photosystem II supercomplexes. *EMBO J.* **28**, 3052 (2009).

586   60.   Kouřil, R. *et al.* Unique organization of photosystem II supercomplexes and

587   megacomplexes in Norway spruce. *Plant J.* **104**, 215–225 (2020).

588   61.   Pribil, M., Labs, M. & Leister, D. Structure and dynamics of thylakoids in land plants. *J.*

589   *Exp. Bot.* **65**, 1955–1972 (2014).

590   62.   Koochak, H., Puthiyaveetil, S., Mullendore, D. L., Li, M. & Kirchhoff, H. The structural

591   and functional domains of plant thylakoid membranes. *Plant J.* **97**, 412–429 (2019).

592   63.   Wood, W. H. J., Barnett, S. F. H., Flannery, S., Hunter, C. N. & Johnson, M. P. Dynamic

593   Thylakoid Stacking Is Regulated by LHCII Phosphorylation but Not Its interaction with

594   PSI. *Plant Physiol.* **180**, 2152–2166 (2019).

595   64.   Ishijima, S., Uchibori, A., Takagi, H., Maki, R. & Ohnishi, M. Light-induced increase in

596   free Mg2+ concentration in spinach chloroplasts: Measurement of free Mg2+ by using a

597   fluorescent probe and necessity of stromal alkalinization. *Arch. Biochem. Biophys.* **412**,

598   126–132 (2003).

599   65.   Izawa, S. & Good, N. E. Effect of Salts and Electron Transport on the Conformation of

600   Isolated Chloroplasts. II. Electron Microscopy. *Plant Physiol.* **41**, 544–552 (1966).

601   66.   Andrew Staehelin, L. Reversible particle movements associated with unstacking and

602   restacking of chloroplast membranes in vitro. *J. Cell Biol.* **71**, 136 (1976).

603   67.   Levitan, O. *et al.* Structural and functional analyses of photosystem II in the marine

604   diatom Phaeodactylum tricornutum. *Proc. Natl. Acad. Sci.* **116**, 17316–17322 (2019).

605   68.   Grinzato, A. *et al.* High-Light versus Low-Light: Effects on Paired Photosystem II

606   Supercomplex Structural Rearrangement in Pea Plants. *Int. J. Mol. Sci. 2020, Vol. 21,*

607   *Page 8643* **21**, 8643 (2020).

608   69.   Albanese, P. *et al.* Pea PSII-LHCII supercomplexes form pairs by making connections

609   across the stromal gap. *Sci. Reports 2017 71* **7**, 1–16 (2017).

610   70.   Yakushevska, A. E. *et al.* The structure of photosystem II in arabidopsis: Localization of

611   the CP26 and CP29 antenna complexes. *Biochemistry* **42**, 608–613 (2003).

612   71.   Zheng, S. Q. *et al.* MotionCor2: Anisotropic correction of beam-induced motion for

613   improved cryo-electron microscopy. *Nature Methods* vol. 14 331–332 (2017).

614   72.   Rohou, A. & Grigorieff, N. CTFFIND4: Fast and accurate defocus estimation from

615   electron micrographs. *J. Struct. Biol.* **192**, 216–221 (2015).

616   73.   Zivanov, J. *et al.* New tools for automated high-resolution cryo-EM structure

617   determination in RELION-3. *Elife* **7**, (2018).

618   74.   Liebschner, D. *et al.* Macromolecular structure determination using X-rays, neutrons and

619   electrons: Recent developments in Phenix. *Acta Crystallogr. Sect. D Struct. Biol.* **75**, 861–

620   877 (2019).

621   75.   Emsley, P., Lohkamp, B., Scott, W. G. & Cowtan, K. Features and development of Coot.

622   *Acta Crystallogr. Sect. D Biol. Crystallogr.* **66**, 486–501 (2010).

623   76.   Chen, V. B. *et al.* MolProbity: All-atom structure validation for macromolecular

624   crystallography. *Acta Crystallogr. Sect. D Biol. Crystallogr.* **66**, 12–21 (2010).

625   77.   Kucukelbir, A., Sigworth, F. J. & Tagare, H. D. The Local Resolution of Cryo-EM

626   Density Maps. *Nat. Methods* **11**, 63 (2014).

627   78.   Pettersen, E. F. *et al.* UCSF Chimera?A visualization system for exploratory research and

628   analysis. *J. Comput. Chem.* **25**, 1605–1612 (2004).

629   79.   Goddard, T. D. *et al.* UCSF ChimeraX: Meeting modern challenges in visualization and

630   analysis. *Protein Sci.* **27**, 14–25 (2018).

631